

Retinex-RAWMamba: Bridging Demosaicing and Denoising for Low-Light RAW Image Enhancement

Xianmin Chen¹, Peiliang Huang², Xiaoxu Feng², Dingwen Zhang², Longfei Han³*, Junwei Han²

¹University of Science and Technology of China

²Northwestern Polytechnical University

³Beijing Technology and Business University

xycarlos@mail.ustc.edu.cn, draftlyhan@gmail.com

Abstract

Low-light image enhancement, particularly in cross-domain tasks such as mapping from the raw domain to the sRGB domain, remains a significant challenge. Many deep learning-based methods have been developed to address this issue and have shown promising results in recent years. However, single-stage methods, which attempt to unify the complex mapping across both domains, leading to limited denoising performance. In contrast, two-stage approaches typically decompose a raw image with color filter arrays (CFA) into a four-channel RGGB format before feeding it into a neural network. However, this strategy overlooks the critical role of demosaicing within the Image Signal Processing (ISP) pipeline, leading to color distortions under varying lighting conditions, especially in low-light scenarios. To address these issues, we design a novel Mamba scanning mechanism, called RAWMamba, to effectively handle raw images with different CFAs. Furthermore, we present a Retinex Decomposition Module (RDM) grounded in Retinex prior, which decouples illumination from reflectance to facilitate more effective denoising and automatic non-linear exposure correction. By bridging demosaicing and denoising, better raw image enhancement is achieved. Experimental evaluations conducted on public datasets SID and MCR demonstrate that our proposed RAWMamba achieves state-of-the-art performance on cross-domain mapping.

Code — <https://github.com/Cynicarlos/RetinexRawMamba>

Introduction

Existing deep learning methods, particularly those focused on low-light enhancement tasks, primarily operate in the sRGB domain. However, RAW images typically possess a higher bit depth than their RGB counterparts, meaning they retain a greater amount of original detail. Consequently, processing from RAW to RGB is often more effective. However, RAW and RGB are distinct domains with image processing algorithms tailored to their specific characteristics. For instance, in the RAW domain, algorithms prioritize denoising, whereas in the RGB domain, they focus on color correction. This difference often renders single-stage end-to-end methods (Maharjan et al. 2019; Gu et al. 2019; Lamba and Mitra 2021) ineffective.

*Corresponding author

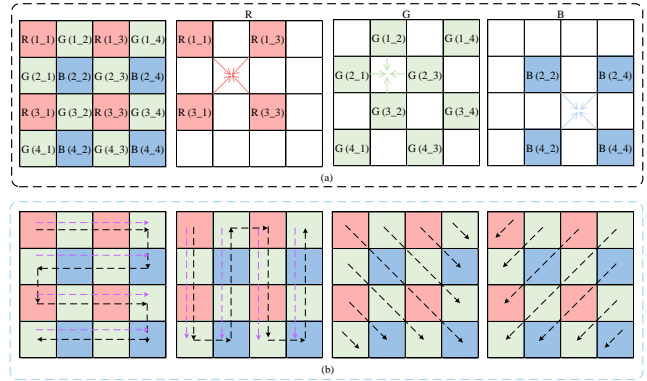


Figure 1: (a) A kind of demosaicing interpolation for RGGB Bayer Pattern and (b) the scanning in RAWMamba (black dashed line) and naive Mamba (purple dashed line). Note that only four directions of RAWMamba are drawn, reversing them gives four more directions, eight in all.

Demosaicing algorithms play a crucial role in converting RAW image to sRGB, with most traditional methods relying on proximity interpolation. Although some researchers have explored CNN-based approaches (Xu et al. 2020; Dong et al. 2022) to map noisy RAW images to clean sRGB outputs, the limited receptive field inherent in convolutional networks often hampers their effectiveness in demosaicing tasks. To address this, Vision Transformers (ViTs) have been employed to expand the receptive field, but the attention mechanisms in ViTs are computationally intensive. The introduction of Mamba provides a more efficient balance between these trade-offs. However, existing Mamba scanning mechanisms do not adequately address the diverse characteristics of RAW images with different Color Filter Arrays (CFAs), highlighting the need for Mamba scanning methods specifically tailored to various CFAs.

Hence, we design a novel Mamba scanning mechanism for RAW format image (RAWMamba), which has a global receptive field and an attention mechanism with linear complexity that can better adapt to the data in this task. More importantly, as shown in Fig. 1 (b), naive Mamba scanning mechanism do not consider imaging properties, leading to limitations in feature extraction with CFA. In contrast, our

RAWMamba introduces eight distinct scanning directions, fully accounting for all pixels in the immediate neighborhood of a given pixel while preserving the spatial continuity of the image. Specifically, the scanning directions encompass horizontal, vertical, oblique scanning from top left to bottom right, and oblique scanning from top right to bottom left. These four primary directions are mirrored to produce an additional four directions, resulting in a total of eight scanning directions.

Additionally, previous methods (Chen et al. 2018; Jin et al. 2023a) for processing short-exposure RAW images often rely on a simple linear multiplication of a prior for exposure correction. Specifically, short-exposure RAW images, which contain significant noise, are multiplied by the exposure time ratio of the corresponding long-exposure image. This approach assumes uniform exposure across the image, which is often unrealistic and can result in sub-optimal denoising and inaccurate brightness. By leveraging the success of the Retinex theory in low-light enhancement tasks for RGB images (Land and McCann 1971; Ma et al. 2022; Sun et al. 2024a), we introduce a Retinex-based dual-domain auxiliary exposure correction method, namely Retinex Decomposition Module (RDM), which decouples illumination and reflection and realize automatic nonlinear exposure correction to achieve more efficient denoising effect and more accurate brightness correction. Furthermore, given the significant differences in noise distribution between different RAW domain and sRGB domain, we build upon the idea of decoupling the task into two sub-tasks: denoising on the raw domain (Yi et al. 2021; Jin et al. 2023b; Wang et al. 2020) and cross-domain mapping (Schwartz, Giryes, and Bronstein 2018; Zamir et al. 2020; Sun et al. 2024b; Ignatov, Van Gool, and Timofte 2020).

In general, we propose a Retinex-based decoupling network (Retinex-RAWMamba) for RAW domain denoising and low-light enhancement shown in Fig. 2. RAWMamba decouples the tasks of denoising and demosaicing into two distinct sub-tasks, effectively mapping noisy RAW images to clean sRGB images. Specifically, for demosaicing sub-task, we introduce RAWMamba to fully consider all pixels in the immediate neighborhood of a certain pixel by utilizing eight direction mechanism. For the denoising sub-task, we propose the Retinex Decomposition Module, which enhances both denoising performance and brightness correction.

Our main contributions are summarized as follows:

- We propose a Retinex-based decoupling Mamba network for RAW domain denoising and low-light enhancement (Retinex-RAWMamba). To our best knowledge, this is first attempt to introduce Mamba mechanism into low-light RAW image task.
- We design a novel eight-direction Mamba scanning mechanism, to thoroughly account for the intrinsic properties of RAW images, and develop a Retinex Decomposition Module to bridging denoising capabilities and exposure correction.
- We evaluate the proposed method on two benchmark datasets quantitatively and qualitatively. The comprehen-

sive experiments show that the proposed method outperforms other state-of-the-art methods in PSNR, SSIM and LPIPS with a comparable number of parameters.

Related Work

Low Light Enhancement on Raw Domain

In the Raw domain low-light enhancement task, researchers have proposed some innovative approaches. Since the task can be split into two sub-tasks, RAW domain denoising and color correction, some of the work only focuses on one of the sub-tasks. For example, on the raw domain denoising task, there are noise modeling with deep learning methods (Bao et al. 2020; Cao et al. 2023; Feng et al. 2024a,b; Wei et al. 2022; Zou and Fu 2022), which ultimately compute evaluation metrics on the raw domain. After the release of the SID public dataset by Chen et al. (Chen et al. 2018) 2018, researchers have proposed many works that address both tasks simultaneously. These works can be further categorized into single-stage approaches and multi-stage approaches. Single-stage methods (Chen et al. 2018; Zamir et al. 2019) aims to map noisy raw to clean sRGB by training a single model. For instance, SID (Chen et al. 2018) only used a simple UNet to accomplish this task. DID (Maharjan et al. 2019) proposed a deep neural network based on residual learning for end-to-end extreme low-light image denoising. SGN (Gu et al. 2019) introduced a self-guided network, which adopted a top-down self-guidance architecture to better exploit image multi-scale information. Since the ISP undergoes many non-linear transformations, it is still difficult to learn for a single neural network, and it can only be realized by piling up a large number of parameters, which leads to inefficiencies, and thus multi-stage methods came into being. Multi-stage methods (Huang et al. 2022; Xu et al. 2020; Zhu et al. 2020) achieve better results by decoupling the tasks, this idea effectively reduces the ambiguity between different domains. For instance, Huang et al. (Huang et al. 2022) proposed intermediate supervision on the raw domain, while Dong et al. (Dong et al. 2022) did that on the monochrome domain. DNF (Jin et al. 2023a) introduced a decoupled two-stage net with weight weight-shared encoder to reduce the number of parameters while achieving good results.

Mamba in Vision Task

State Space Models (SSM) are recently introduced to deep learning since they can effectively model long range dependencies. For instance, (Gu, Goel, and Ré 2022) proposes a Structured State-Space Sequence (S4) model and recently, (Gu and Dao 2023) proposes Mamba, which outperforms Transformers at various sizes on large-scale real data and enjoys linear scaling in sequence length. In addition to Mamba’s great work on NLP tasks, researchers have also made many attempts and achieved good results on visual tasks, such as classification (Chen et al. 2024; Yue and Li 2024), segmentation (Ma, Li, and Wang 2024; Wang et al. 2024; Xing et al. 2024; Ruan and Xiang 2024; Liu et al. 2024a), generation (Shen et al. 2024; Hu et al. 2024), and image restoration (Guo et al. 2024; Shi et al. 2024; Zhen, Hu, and Feng 2024; Zheng and Wu 2024; Pei, Huang, and

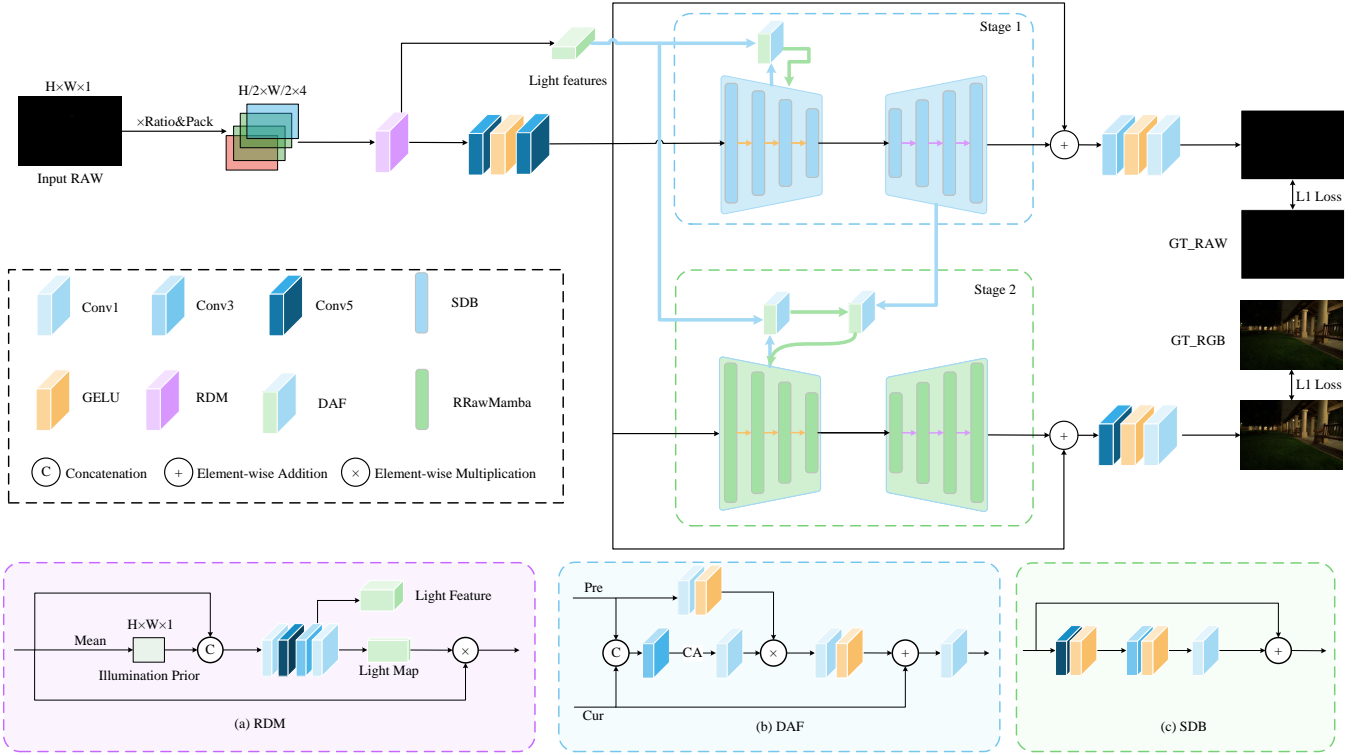


Figure 2: The overall architecture of our proposed Retinex-RAWMamba and (a) Retinex Decomposition Module, (b) Domain Adaptive Fusion and (c) Simple Denoising Block

Xu 2024; Bai et al. 2024). EfficientVMamba (Pei, Huang, and Xu 2024) presents the Efficient 2D Scanning (ES2D) method, utilizing atrous sampling of patches on the feature map to speed up training. VMamba (Liu et al. 2024b) incorporates a Cross-Scan Module (CSM), which converts the input image into sequences of patches along the horizontal and vertical axes, and it enables the scanning of sequences in four distinct directions. That is, each pixel integrates information from the four surrounding pixels. FreqMamba (Zhen, Hu, and Feng 2024) introduces complementary triple interaction structures including spatial Mamba, frequency band Mamba, and Fourier global modeling, which utilizes the complementarity between Mamba and frequency analysis for image deraining.

Method

Preliminaries

State Space Model (SSM) SSM is a linear time-invariant system that maps input $x(t) \in \mathbb{R}^L$ to output $y(t) \in \mathbb{R}^L$. SSM can be formally represented by a linear ordinary differential equation (ODE),

$$\begin{aligned} h'(t) &= \mathbf{A}h(t) + \mathbf{B}x(t), \\ y(t) &= \mathbf{C}h(t) + \mathbf{D}x(t) \end{aligned} \quad (1)$$

SSM is continuous-time model, presenting significant challenges when integrated into deep learning algorithms. To address this issue, discretization becomes a crucial step.

Denote Δ as the timescale parameter. The zero-order hold (ZOH) rule is usually used for discretization to convert continuous parameters \mathbf{A} and \mathbf{B} in Eq.1 into discrete parameters $\bar{\mathbf{A}}$ and $\bar{\mathbf{B}}$. Its definition is as follows:

$$\begin{aligned} \bar{\mathbf{A}} &= \exp(\Delta\mathbf{A}), \\ \bar{\mathbf{B}} &= (\Delta\mathbf{A})^{-1}(\exp(\Delta\mathbf{A}) - \mathbf{I}) \cdot \Delta\mathbf{B} \end{aligned} \quad (2)$$

After the discretization of \mathbf{A} , \mathbf{B} , the discretized version of Eq. 1 using a step size Δ can be rewritten as:

$$\begin{aligned} h_k &= \bar{\mathbf{A}}h_{k-1} + \bar{\mathbf{B}}x_k, \\ y_k &= \mathbf{C}h_k + \mathbf{D}x_k \end{aligned} \quad (3)$$

Finally, the models compute output through a global convolution as following:

$$\begin{aligned} \bar{\mathbf{K}} &= (\mathbf{C}\bar{\mathbf{B}}, \mathbf{C}\bar{\mathbf{A}}\bar{\mathbf{B}}, \dots, \mathbf{C}\bar{\mathbf{A}}^{L-1}\bar{\mathbf{B}}) \\ \mathbf{y} &= \mathbf{x} * \bar{\mathbf{K}} \end{aligned} \quad (4)$$

where L is the length of the input sequence \mathbf{x} , and $\bar{\mathbf{K}} \in \mathbb{R}^L$ is a structured convolutional kernel.

Overall Pipeline

The overall pipeline is shown in Fig. 2. First, we preprocess the low-exposure noisy single-channel raw image by multiplying it with the exposure time ratio of the long-exposure ground truth (GT). Then, based on the Color Filter

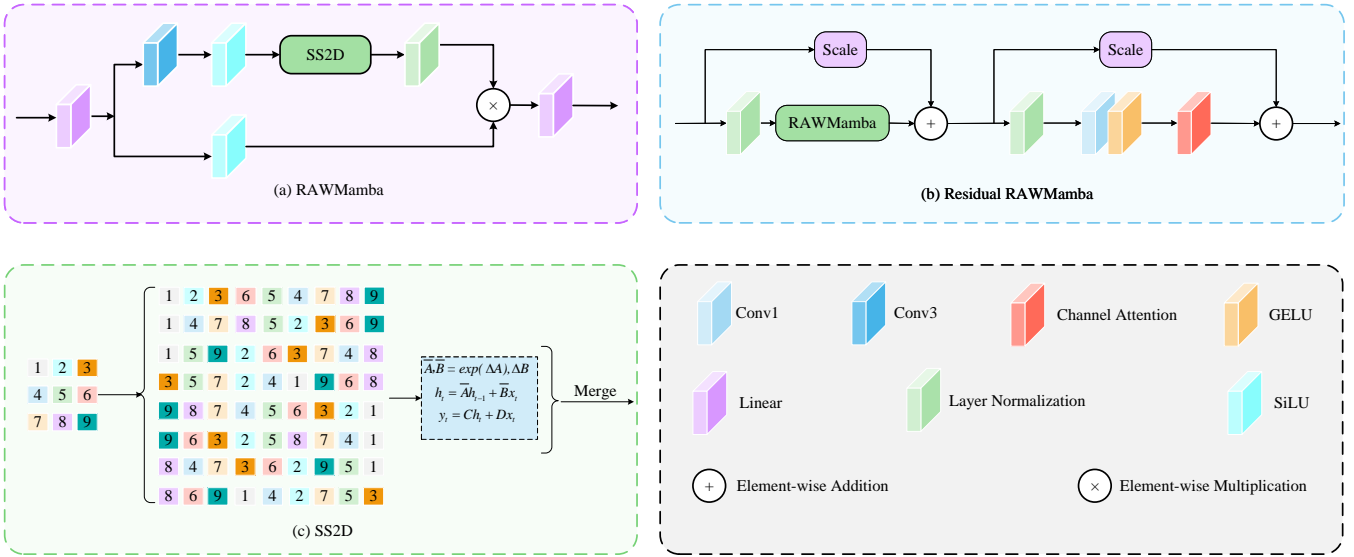


Figure 3: Details of (a) RAWMamba, (b) Residual RAWMamba and (c) SS2D

Array (CFA) pattern, we pack it into a multi-channels input. Specifically, for Bayer format, we pack the input $\mathbf{X} \in \mathbb{R}^{H \times W \times 1}$ into four channels input $\mathbf{X}_{packed} \in \mathbb{R}^{\frac{H}{2} \times \frac{W}{2} \times 4}$, for XTrans format, we pack the input into nine channels input $\mathbf{X}_{packed} \in \mathbb{R}^{\frac{H}{3} \times \frac{W}{3} \times 9}$. Both stages of Retinex-RAWMamba are built upon the UNet-based (Ronneberger, Fischer, and Brox 2015) encoder-decoder architecture. The first stage of the overall framework is dedicated to raw domain denoising. Initially, The Retinex Decomposition Module (RDM) processes the input to generate both the primary input and an auxiliary illumination feature map, denoted as \mathbf{I} . This primary input is then fused with \mathbf{I}_i at each encoding layer and denoised using the Simple Denoising Block (SDB), which consists of three consecutive convolutions followed by a residual connection. At each decoding layer, a temporary feature map \mathbf{f}_i is generated, ultimately resulting in the generation of the denoised raw image. The loss function for the first stage is computed against the ground truth RAW image, which also serves as the supervision signal for this stage. In the second stage, the focus shifts to demosaicing and color correction. In this phase, the input is fused with both \mathbf{I}_i and \mathbf{f}_i , and processed by the RAWMamba at each layer. After decoding, the final RGB image is produced. The loss function is then calculated against the ground truth RGB image, providing the supervision signal for this stage and guiding the optimization of whole model.

RAWMamba

The details of RAWMamba and Residual RAWMamba are shown in Fig. 3. RAWMamba leverages the naive visual mamba in MambaIR (Guo et al. 2024), with an innovative scanning mechanism. In the ISP process from Raw to RGB, proximity interpolation is commonly employed for demosaicing and often involves considering all eight closely connected locations around a given position, and Fig.1 (a) gives an example with Bayer pattern raw image, (b) shows

the scanning in RAWMamba (black dashed line) and naive Mamba (purple dashed line). The naive scanning method fails to consider the continuity of scanning, resulting in a lack of continuity between the end of each row/column and its bottom/right side. This leads to gaps in image semantics, which hinders image reconstruction. To address this issue, we propose using a Z-scan. That is, when the scan reaches the end of each row/column, the reverse scan starts from the next row/column immediately adjacent to the last pixel. However, there are still limitations with this scanning method as it does not take into account all eight surrounding pixels when certain pixels are close to each other at the top, bottom, left, and right positions. Taking into consideration the characteristics of this task, we introduce Eight direction Mamba.

The detail of the our proposed scan mechanism is shown in 3 (c). Specifically, for a feature map $\mathbf{F} \in \mathbb{R}^{C \times H \times W}$, we first flip its even rows (fer) and columns (fec) to get $\mathbf{F}_{fer} \in \mathbb{R}^{C \times H \times W}$ and $\mathbf{F}_{fec} \in \mathbb{R}^{C \times H \times W}$, respectively. Then we flatten \mathbf{F}_{fer} and \mathbf{F}_{fec} to get the first tow directions' scanning $\mathbf{F}_1 \in \mathbb{R}^{C \times HW}$ and $\mathbf{F}_2 \in \mathbb{R}^{C \times HW}$. Then we can get the feature of the oblique scan \mathbf{F}_3 as following:

$$\begin{aligned}
 (r, c) &= (\text{ceil}(\frac{H \times W}{W + 1}), (W + 1)) \\
 \mathbf{F}_{pad} &= \text{pad}(\text{flatten}(\mathbf{F}), (C, r \times c)) \\
 \mathbf{F}_{reshaped} &= \text{reshape}(\mathbf{F}_{pad}, (C, r, c)) \\
 \mathbf{F}_{select} &= \text{ms}(\text{trans}(\mathbf{F}_{reshaped}), \text{trans}(\mathbf{mask})) \\
 \mathbf{F}_3 &= \text{reshape}(\mathbf{F}_{select}, (C, H \times W))
 \end{aligned} \tag{5}$$

where $\text{pad}(\mathbf{X}, \text{shape})$ is a function to pad \mathbf{X} to new shape, \mathbf{mask} and $\mathbf{F}_{reshaped}$ have the same shape, and the first $H \times W$ elements of \mathbf{mask} are true and the rest are false, $\text{trans}(\mathbf{X})$ is a function to transpose $\mathbf{X} \in \mathbb{R}^{C \times H \times W}$ to $\mathbf{X}_{trans} \in \mathbb{R}^{C \times W \times H}$, $\text{ms}(\mathbf{X}, \mathbf{mask})$ is a function to select elements from \mathbf{X} based on the position where \mathbf{mask} is true.

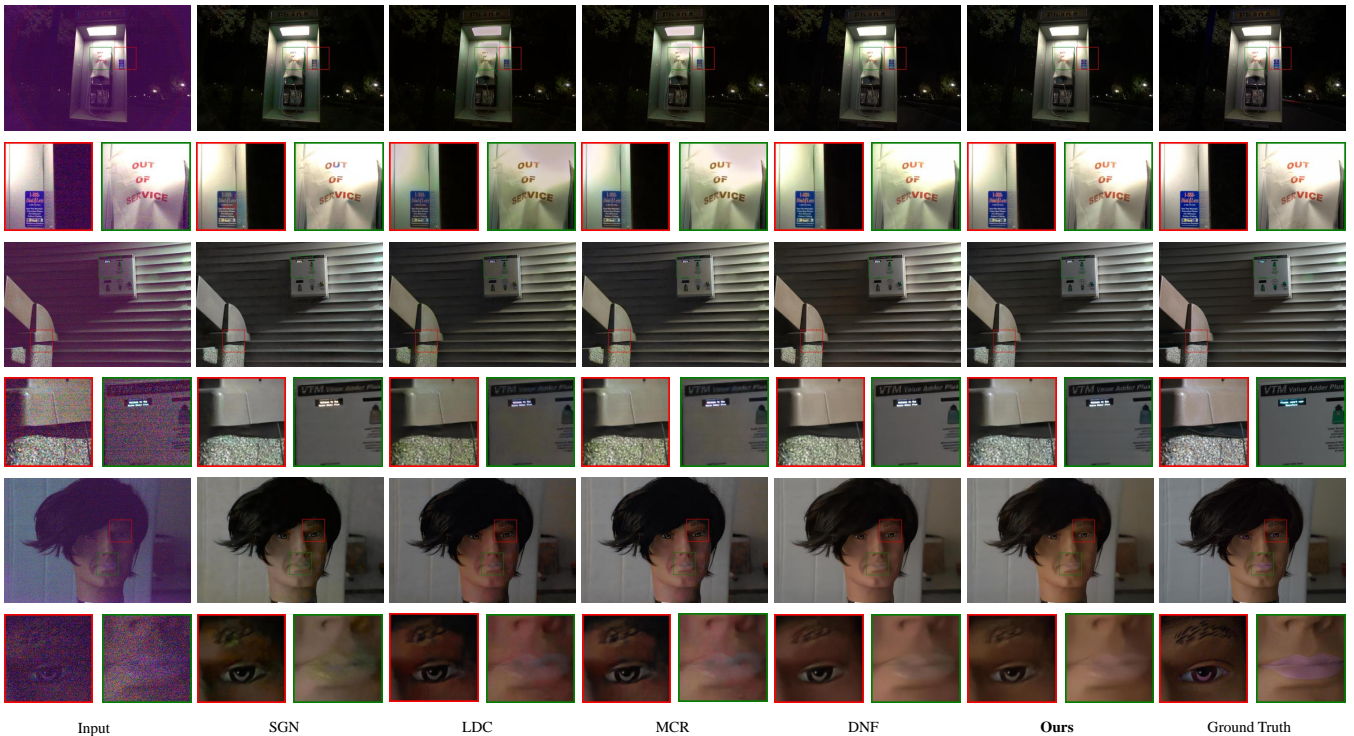


Figure 4: The visualization results between our method and the state-of-the-art methods (Zoom-in for best view).

The other oblique scan feature F_4 can be obtained similarly, and then we can invert these four features to get another four directions features, eight in total, which is $\{F_i \in \mathbb{R}^{C \times HW}, i = 1, 2, \dots, 8\}$. At this point, the scanning of the eight directions is completed. And after the SSM, we get $\{\bar{F}_i \in \mathbb{R}^{C \times HW}, i = 1, 2, \dots, 8\}$, we then merge them by adding them up and reshape these eight features to the original shape to get a single feature, that is,

$$RAWMamba(F) = Reshape\left(\sum_{i=1}^8 \bar{F}_i, (C, H, W)\right) \quad (6)$$

For the proposed Residual RAWMamba, It can be simply formulated as:

$$\begin{aligned} T &= \alpha X + RAWMamba(LN(X)) \\ Out &= \beta T + CA(GELU(Conv(LN(T)))) \end{aligned} \quad (7)$$

where, LN is layer normalization, α and β are parameters that can be learned, CA is channel attention.

Retinex Decomposition

Low-light enhancement methods based on retinex theory have been successful in RGB domain (Wei et al. 2018; Wu et al. 2022; Cai et al. 2023), so we propose dual-domain Retinex Decomposition Module. RDM can decompose image $X \in \mathbb{R}^{H \times W \times C}$ into the reflection component $R \in \mathbb{R}^{H \times W \times C}$ and the illumination component $I \in \mathbb{R}^{H \times W \times C}$. The details of RDM are shown in Fig. 2 (a). The module first takes the average value of the input image $X \in \mathbb{R}^{H \times W \times C}$

in the channel dimension to obtain $M \in \mathbb{R}^{H \times W \times 1}$, concatenates them in the channel dimension, and then passes several convolutions to obtain the first output light feature $I \in \mathbb{R}^{H \times W \times C}$, and then passes a 1×1 convolution to obtain the light map, and finally light map will be multiplied by the original input X to obtain the second output reflection map R after a 1×1 convolution. Specifically,

$$\begin{aligned} I &= Conv_{1,5,3}\{cat[X, sap(X)]\} \\ R &= X \odot Conv_1(I) \end{aligned} \quad (8)$$

where sap donates Spatial Average Pooling, cat refers to the concatenation of tow feature maps on the channel dimension, $Conv_{1,5,3}$ donates a series of convolution with kernel size 1, 5 and 3, \odot is the Hadamard product. And after obtaining the light feature I , we will simply downsample it to get four feature maps at each layer, which are donated as $\{I_f^i, i = 1, 2, 3, 4\}$, I_f^i is the i_{th} layer light feature that will be fused later for auxiliary automatic exposure correction at layer i .

Domain Adaptive Fusion

The details of DAF are shown in Fig. 2 (b), previous feature map will be firstly concatenated with current feature map at the same level, and this result will be multiplied with previous feature map after the convolution, then it will pass through a convolution with a residual addition. And we can get the fused feature map after a final convolution. Specifically, for the tow feature maps $pre \in \mathbb{R}^{H \times W \times C}$ and $cur \in \mathbb{R}^{H \times W \times C}$, they will be fused as following:

Table 1: Quantitative results of RAW-based LLIE methods on the Sony and Fuji subsets of SID. The top-performing result is highlighted in **bold**, while the second-best is shown in underline. Metrics marked with \uparrow indicate that a higher value is better, and those marked with \downarrow indicate that a lower value is better. N/A indicates the result is not available.

Category	Method	Venue	#Params.(M)	Sony			Fuji		
				PSNR \uparrow	SSIM \uparrow	LPIPS \downarrow	PSNR \uparrow	SSIM \uparrow	LPIPS \downarrow
Single-Stage	SID	CVPR2018	7.7	28.96	0.787	0.356	26.66	0.709	0.432
	DID	ICME2019	2.5	29.16	0.785	0.368	N/A	N/A	N/A
	SGN	ICCV2019	19.2	29.28	0.790	0.370	27.41	0.720	0.430
	LLPackNet	BMVC2020	1.2	27.83	0.755	0.541	N/A	N/A	N/A
	RRT	CVPR2021	0.8	28.66	0.790	0.397	26.94	0.712	0.446
Multi-Stage	EEMEFN	AAAI2020	40.7	29.60	0.795	0.350	27.38	0.723	0.414
	LDC	CVPR2020	8.6	29.56	<u>0.799</u>	0.359	27.18	0.703	0.446
	MCR	CVPR2022	15.0	29.65	0.797	0.348	N/A	N/A	N/A
	RRENet	TIP2022	15.5	29.17	0.792	0.360	27.29	0.720	0.421
	DNF	CVPR2023	2.8	<u>30.62</u>	0.797	<u>0.343</u>	<u>28.71</u>	<u>0.726</u>	<u>0.391</u>
	Ours	-	6.2	30.76	0.810	0.328	29.02	0.743	0.382

$$\begin{aligned}
 \mathbf{T} &= \text{Conv}_3(\text{cat}(\mathbf{pre}, \mathbf{cur})) \\
 \mathbf{T} &= \text{Conv}_1(\text{CA}(\mathbf{T})) \\
 \mathbf{T} &= \mathbf{T} \odot \text{Conv}_1(\text{GELU}(\mathbf{pre})) \\
 \mathbf{T} &= \text{Conv}_1(\text{GELU}(\mathbf{T})) \\
 \text{Out}(\mathbf{cur}, \mathbf{pre}) &= \text{Conv}_1(\mathbf{T} + \mathbf{cur})
 \end{aligned} \tag{9}$$

Loss Function

Traditional low-level vision tasks generally use L1 Loss, and we also follow that, but our task involves different sub-tasks on two domains, Raw domain and sRGB domain, so the loss can be expressed as following:

$$\begin{aligned}
 L_{total} &= \alpha L_{raw} + \beta L_{srgb} \\
 &= \alpha \|\hat{Y}_{raw} - GT_{raw}\|_1 + \beta \|\hat{Y}_{srgb} - GT_{srgb}\|_1
 \end{aligned}$$

where Y_{raw} is the raw image after denoised, Y_{srgb} is the sRGB image after the second stage, GT_{srgb} is the sRGB image obtained from raw ground truth after post-processing by Rawpy as previous work did. And α and β defaults to 1.0 in our experiments.

Experiments

Datasets and Experiments Environments

SID Dataset For Sony subset, there are totally 1865 raw image pairs in the training set. Each pair of images contains a short exposure and a long exposure, the short exposure is used as noisy raw, and the long exposure is used as GT_{raw} . The original size of all images is 2848×4256 . Limited by GPU memory, the data is preprocessed before training, first pack into $4 \times 1424 \times 2128$, then randomly crop a patch with shape $4 \times 512 \times 512$ as the input with random data augmentation, such as horizontal/vertical flipping. For the test set, we referred to the DNF(Jin et al. 2023a) settings and deleted the three misaligned scene images.

For Fuji subset, similar to Sony subset, 1655 and 524 raw

image pairs for training and testing, respectively. The original size of it is 4032×6032 , since its CFA (Color Filter Array) is X-Trans instead of Bayer, we pack it into $9 \times 1344 \times 2010$ and randomly crop a patch with shape $9 \times 384 \times 384$ as the input.

MCR Dataset The MCR (Dong et al. 2022) dataset contains 4980 images with a resolution of 1280×1024 , including 3984 low-light RAW images, 498 monochrome images (not be used for us) and 498 sRGB images. With indoor and outdoor scenes, different exposure times are set, 1/256s to 3/8s for indoor scenes and 1/4096s to 1/32s for outdoor scenes. And we obtained the raw ground truth as DNF (Jin et al. 2023a) did. The preprocessing is similar to SID dataset, but we don't randomly crop a patch as the input.

Implementation Details During training, the batch size is 1 and the initial learning rate is $1e-4$, and we use the cosine annealing strategy to reduce it to $1e-5$ at the 200th epoch. Adamw optimizer is used and the betas parameter is [0.9,0.999] and the momentum is 0.9. The training and testing is completed by a NVIDIA 3090 (24G), A40 (48G), respectively due to the limitation of GPU memory. We also provide the code of merging test on a 24G GPU. Note that the results of merging test are a litter bit smaller than that testing with whole image. And we use PSNR, SSIM (Wang et al. 2004) and LPIPS (Zhang et al. 2018) as the quantitative evaluation metrics.

Comparison with State-of-the-Arts

We conduct experiments on SID (Chen et al. 2018) dataset including Sony and Fuji subsets and MCR (Dong et al. 2022) dataset, and compare with previous SOTA methods including SID (Chen et al. 2018), DID (Maharjan et al. 2019), SGN (Gu et al. 2019), EEMEFN (Zhu et al. 2020), LDC (Xu et al. 2020), LLPackNet (Lamba, Balaji, and Mitra 2020), RRT (Lamba and Mitra 2021), MCR (Dong et al. 2022), RRENet (Huang et al. 2022) and DNF (Jin et al. 2023a).

Table 2: Quantitative results on MCR (Dong et al. 2022) dataset. The top-performing result is highlighted in **bold**, while the second-best is shown in underline. Metrics marked with \uparrow indicate that a higher value is better, and those marked with \downarrow indicate that a lower value is better.

Category	Method	PSNR \uparrow	SSIM \uparrow
Single-Stage	SID	29.00	0.906
	DID	26.16	0.888
	SGN	26.29	0.882
	RRT	25.74	0.851
Multi-Stage	LDC	29.36	0.904
	MCR	31.69	0.908
	DNF	<u>32.00</u>	0.915
	Ours	33.14	<u>0.914</u>

The results are presented in Tab. 1 and 2. As observed, most single-stage methods underperform compared to multi-stage methods, demonstrating the feasibility and effectiveness of the multi-stage approach for noisy RAW to clean sRGB cross-domain mapping. On the SID dataset, our proposed method outperforms all metrics among multi-stage approaches, while maintaining a smaller parameter count. Specifically, on the Sony and Fuji subsets, our method achieves a PSNR increase of 0.14 dB and 0.31 dB, respectively, an SSIM improvement of 0.011 and 0.017, and an LPIPS reduction of 0.015 and 0.009, compared to the best existing method.

For the MCR dataset, as shown in Tab. 2, while our improvement in SSIM is modest, we achieve a significant PSNR increase of 1.14 dB, a 3.6% enhancement over the second-best method. Additionally, we selected several previous state-of-the-art (SOTA) methods and visualized their performance on the SID Sony dataset, as shown in Fig. 4. Three scenarios are depicted, each containing two sub-regions. In the first two scenes, most other methods produce a green tint to the image. In the third scene, these methods often fail to preserve details adequately. In contrast, our proposed method closely aligns with the ground truth in both color and detail, effectively achieving denoising and color enhancement in the raw domain under low-light conditions.

Ablation Studies

To demonstrate the validity of our proposed method, we perform ablation experiments on the SID Sony dataset. We first propose a baseline model that consists only of SDB and the unmodified naive visual mamba and GFM from DNF (Jin et al. 2023a). Tab. 3 shows the results of adding or replacing the corresponding module based on the baseline, where RRAWM stands for replacing naive Mamba with RRAWMamba, RDM stands for adding RDM module, and DAF stands for replacing GFM with DAF module. All the ablation experiments were conducted in the same environment.

First, we replaced the baseline’s naive Mamba with the proposed RRAWMamba. The results showed increases of 0.41 dB in PSNR and 0.012 in SSIM, demonstrating that our

Table 3: Ablation study on SID Sony dataset.

Baseline	RRAWM	RDM	DAF	PSNR	SSIM
\checkmark				30.04	0.797
	\checkmark			30.45	0.809
	\checkmark	\checkmark		30.72	0.809
	\checkmark	\checkmark	\checkmark	30.76	0.810

RRAWMamba, with its eight-directional scanning mechanism, performs well in the demosaicing task. Next, we incorporated the proposed RDM for denoising and automatic exposure correction. The results indicated that although SSIM did not improve, PSNR increased by an additional 0.27 dB. This suggests that the initial exposure of the images was indeed problematic, and our RDM effectively enhances denoising and exposure correction. Finally, we replaced all GFM components in the network with our proposed DAF to improve the stability of the training process. This led to further gains, with PSNR and SSIM increasing by 0.04 dB and 0.001, respectively.

Additionally, we performed a simple visualization of the ablation study, as shown in Fig. 5. The use of RRAWMamba in the baseline enhances dark image details, though brightness remains insufficient. Retinex-RawMamba with RDM addresses this issue, and it is evident that our proposed method achieves better results in both detail and brightness in extremely dark areas.

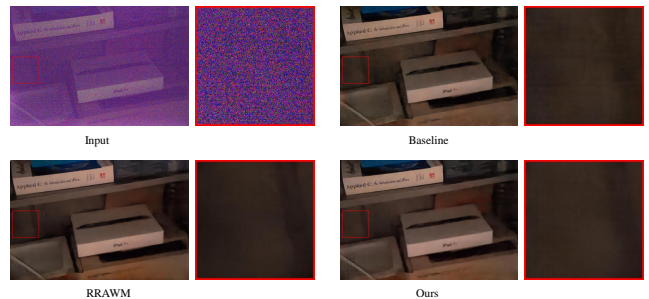


Figure 5: The visualization results for ablation studies (Zoom-in for best view).

Conclusion

For the task of denoising and enhancing RAW images under low-light conditions, we introduce Retinex-RAWMamba, a novel two-stage cross-domain network. Our approach extends the capabilities of the traditional Vision Mamba by incorporating RAWMamba, which exploits the inherent properties of demosaicing algorithms in ISP to achieve enhanced color correction and detail retention. Additionally, we integrate Retinex theory through our Retinex Decomposition Module, facilitating automatic exposure correction and yielding RGB images with improved illumination and brightness fidelity. Comprehensive theoretical analysis and experimental validation underscore the effectiveness and significant potential of our method.

References

- Bai, J.; Yin, Y.; He, Q.; Li, Y.; and Zhang, X. 2024. Retinexmamba: Retinex-based Mamba for Low-light Image Enhancement. arXiv:2405.03349.
- Bao, L.; Yang, Z.; Wang, S.; Bai, D.; and Lee, J. 2020. Real Image Denoising Based on Multi-Scale Residual Dense Block and Cascaded U-Net with Block-Connection. In *CVPRW*, 1823–1831.
- Cai, Y.; Bian, H.; Lin, J.; Wang, H.; Timofte, R.; and Zhang, Y. 2023. Retinexformer: One-stage Retinex-based Transformer for Low-light Image Enhancement. In *ICCV*, 12504–12513.
- Cao, Y.; Liu, M.; Liu, S.; Wang, X.; Lei, L.; and Zuo, W. 2023. Physics-guided iso-dependent sensor noise modeling for extreme low-light photography. In *CVPR*, 5744–5753.
- Chen, C.; Chen, Q.; Xu, J.; and Koltun, V. 2018. Learning to see in the dark. In *CVPR*, 3291–3300.
- Chen, K.; Chen, B.; Liu, C.; Li, W.; Zou, Z.; and Shi, Z. 2024. RSMamba: Remote Sensing Image Classification with State Space Model. arXiv:2403.19654.
- Dong, X.; Xu, W.; Miao, Z.; Ma, L.; Zhang, C.; Yang, J.; Jin, Z.; Teoh, A. B. J.; and Shen, J. 2022. Abandoning the Bayer-Filter To See in the Dark. In *CVPR*, 17431–17440.
- Feng, H.; Wang, L.; Huang, Y.; Wang, Y.; Zhu, L.; and Huang, H. 2024a. Physics-guided Noise Neural Proxy for Practical Low-light Raw Image Denoising. arXiv:2310.09126.
- Feng, H.; Wang, L.; Wang, Y.; Fan, H.; and Huang, H. 2024b. Learnability Enhancement for Low-Light Raw Image Denoising: A Data Perspective. *IEEE TPAMI*, 46(01): 370–387.
- Gu, A.; and Dao, T. 2023. Mamba: Linear-Time Sequence Modeling with Selective State Spaces. arXiv:2312.00752.
- Gu, A.; Goel, K.; and Ré, C. 2022. Efficiently Modeling Long Sequences with Structured State Spaces. arXiv:2111.00396.
- Gu, S.; Li, Y.; Van Gool, L.; and Timofte, R. 2019. Self-Guided Network for Fast Image Denoising. In *ICCV*, 2511–2520.
- Guo, H.; Li, J.; Dai, T.; Ouyang, Z.; Ren, X.; and Xia, S.-T. 2024. MambaIR: A Simple Baseline for Image Restoration with State-Space Model. arXiv:2402.15648.
- Hu, V. T.; Baumann, S. A.; Gui, M.; Grebenkova, O.; Ma, P.; Fischer, J.; and Ommer, B. 2024. ZigMa: A DiT-style Zigzag Mamba Diffusion Model. arXiv:2403.13802.
- Huang, H.; Yang, W.; Hu, Y.; Liu, J.; and Duan, L.-Y. 2022. Towards Low Light Enhancement With RAW Images. *IEEE TIP*, 31: 1391–1405.
- Ignatov, A.; Van Gool, L.; and Timofte, R. 2020. Replacing Mobile Camera ISP with a Single Deep Learning Model. In *CVPRW*, 2275–2285.
- Jin, X.; Han, L.-H.; Li, Z.; Guo, C.-L.; Chai, Z.; and Li, C. 2023a. DNF: Decouple and Feedback Network for Seeing in the Dark. In *CVPR*, 18135–18144.
- Jin, X.; Xiao, J.-W.; Han, L.-H.; Guo, C.; Zhang, R.; Liu, X.; and Li, C. 2023b. Lighting Every Darkness in Two Pairs: A Calibration-Free Pipeline for RAW Denoising. In *ICCV*.
- Lamba, M.; Balaji, A.; and Mitra, K. 2020. Towards Fast and Light-Weight Restoration of Dark Images. arXiv:2011.14133.
- Lamba, M.; and Mitra, K. 2021. Restoring Extremely Dark Images in Real Time. In *CVPR*, 3486–3496.
- Land, E. H.; and McCann, J. J. 1971. Lightness and retinex theory. *Journal of the Optical Society of America*, 61 1: 1–11.
- Liu, J.; Yang, H.; Zhou, H.-Y.; Xi, Y.; Yu, L.; Yu, Y.; Liang, Y.; Shi, G.; Zhang, S.; Zheng, H.; and Wang, S. 2024a. Swin-UMamba: Mamba-based UNet with ImageNet-based pre-training. arXiv:2402.03302.
- Liu, Y.; Tian, Y.; Zhao, Y.; Yu, H.; Xie, L.; Wang, Y.; Ye, Q.; and Liu, Y. 2024b. VMamba: Visual State Space Model. arXiv:2401.10166.
- Ma, J.; Li, F.; and Wang, B. 2024. U-Mamba: Enhancing Long-range Dependency for Biomedical Image Segmentation. arXiv:2401.04722.
- Ma, L.; Ma, T.; Liu, R.; Fan, X.; and Luo, Z. 2022. Toward Fast, Flexible, and Robust Low-Light Image Enhancement. In *CVPR*, 5637–5646.
- Maharjan, P.; Li, L.; Li, Z.; Xu, N.; Ma, C.; and Li, Y. 2019. Improving Extreme Low-Light Image Denoising via Residual Learning. In *ICME*, 916–921.
- Pei, X.; Huang, T.; and Xu, C. 2024. EfficientVMamba: Atrous Selective Scan for Light Weight Visual Mamba. arXiv:2403.09977.
- Ronneberger, O.; Fischer, P.; and Brox, T. 2015. U-net: Convolutional networks for biomedical image segmentation. In *Medical image computing and computer-assisted intervention—MICCAI 2015: 18th international conference, Munich, Germany, October 5-9, 2015, proceedings, part III 18*, 234–241. Springer.
- Ruan, J.; and Xiang, S. 2024. VM-UNet: Vision Mamba UNet for Medical Image Segmentation. arXiv:2402.02491.
- Schwartz, E.; Giryes, R.; and Bronstein, A. M. 2018. Deepisp: Toward learning an end-to-end image processing pipeline. *IEEE TIP*, 28(2): 912–923.
- Shen, Q.; Wu, Z.; Yi, X.; Zhou, P.; Zhang, H.; Yan, S.; and Wang, X. 2024. Gamba: Marry Gaussian Splatting with Mamba for single view 3D reconstruction. arXiv:2403.18795.
- Shi, Y.; Xia, B.; Jin, X.; Wang, X.; Zhao, T.; Xia, X.; Xiao, X.; and Yang, W. 2024. VmambaIR: Visual State Space Model for Image Restoration. arXiv:2403.11423.
- Sun, S.; Ren, W.; Peng, J.; Song, F.; and Cao, X. 2024a. DI-Retinex: Digital-Imaging Retinex Theory for Low-Light Image Enhancement. arXiv:2404.03327.
- Sun, X.; Zhao, Z.; Wei, L.; Lang, C.; Cai, M.; Han, L.; Wang, J.; Li, B.; and Guo, Y. 2024b. RL-SeqISP: Reinforcement Learning-Based Sequential Optimization for Image Signal Processing. In *AAAI*, 5025–5033. AAAI Press.

Wang, Y.; Huang, H.; Xu, Q.; Liu, J.; Liu, Y.; and Wang, J. 2020. Practical Deep Raw Image Denoising on Mobile Devices. In *ECCV*, 1–16.

Wang, Z.; Bovik, A.; Sheikh, H.; and Simoncelli, E. 2004. Image quality assessment: from error visibility to structural similarity. *IEEE TIP*, 13(4): 600–612.

Wang, Z.; Zheng, J.-Q.; Zhang, Y.; Cui, G.; and Li, L. 2024. Mamba-UNet: UNet-Like Pure Visual Mamba for Medical Image Segmentation. arXiv:2402.05079.

Wei, C.; Wang, W.; Yang, W.; and Liu, J. 2018. Deep Retinex Decomposition for Low-Light Enhancement. In *BMVC*.

Wei, K.; Fu, Y.; Zheng, Y.; and Yang, J. 2022. Physics-Based Noise Modeling for Extreme Low-Light Photography. *IEEE TPAMI*, 44(11): 8520–8537.

Wu, W.; Weng, J.; Zhang, P.; Wang, X.; Yang, W.; and Jiang, J. 2022. URetinex-Net: Retinex-based Deep Unfolding Network for Low-light Image Enhancement. In *CVPR*, 5891–5900.

Xing, Z.; Ye, T.; Yang, Y.; Liu, G.; and Zhu, L. 2024. SegMamba: Long-range Sequential Modeling Mamba For 3D Medical Image Segmentation. arXiv:2401.13560.

Xu, K.; Yang, X.; Yin, B.; and Lau, R. W. 2020. Learning to Restore Low-Light Images via Decomposition-and-Enhancement. In *CVPR*, 2278–2287.

Yi, Z.; Qin, H.; Wang, X.; and Li, H. 2021. Rethinking Noise Synthesis and Modeling in Raw Denoising. In *ICCV*, 4593–4601.

Yue, Y.; and Li, Z. 2024. MedMamba: Vision Mamba for Medical Image Classification. arXiv:2403.03849.

Zamir, S. W.; Arora, A.; Khan, S.; Hayat, M.; Khan, F. S.; Yang, M.-H.; and Shao, L. 2020. Cycleisp: Real image restoration via improved data synthesis. In *CVPR*, 2696–2705.

Zamir, S. W.; Arora, A.; Khan, S.; Khan, F. S.; and Shao, L. 2019. Learning Digital Camera Pipeline for Extreme Low-Light Imaging. arXiv:1904.05939.

Zhang, R.; Isola, P.; Efros, A. A.; Shechtman, E.; and Wang, O. 2018. The unreasonable effectiveness of deep features as a perceptual metric. In *CVPR*, 586–595.

Zhen, Z.; Hu, Y.; and Feng, Z. 2024. FreqMamba: Viewing Mamba from a Frequency Perspective for Image Deraining. arXiv:2404.09476.

Zheng, Z.; and Wu, C. 2024. U-shaped Vision Mamba for Single Image Dehazing. arXiv:2402.04139.

Zhu, M.; Pan, P.; Chen, W.; and Yang, Y. 2020. EEMEFN: Low-Light Image Enhancement via Edge-Enhanced Multi-Exposure Fusion Network. *AAAI*, 34: 13106–13113.

Zou, Y.; and Fu, Y. 2022. Estimating Fine-Grained Noise Model via Contrastive Learning. In *CVPR*, 12672–12681.